Supporting Information

Electronic structure manipulation via composition tuning for the development of highly conductive and acid-stable oxides

Young-Woon Byeon,[a] Jonathan Mailoa,[b] Mordechai Kornbluth,[b] Gi-Hyeok Lee,[c] Zijian Cai,[a,d] Yingzhi Sun,[a,d] Wanli Yang,[c] Christina Johnston,[e] Jake Christensen,[e] Soo Kim,*[b] Lei Cheng*[e] and Haegyeom Kim*[a]

[a]Materials and Sciences Division, Lawrence Berkeley National Laboratory, 1 Cyclotron Rd, Berkeley, CA 94720, USA

[b]Research and Technology Center, Robert Bosch LLC, 1 Kendall Square Suite 7-101, Cambridge, MA 02139, USA

[c]Advanced Light Source, Lawrence Berkeley National Laboratory, Berkeley, CA 94720, USA

[d]Department of Materials Science and Engineering, University of California Berkeley, Berkeley, CA 94704, USA

[e]Research and Technology Center, Robert Bosch LLC, 384 Santa Trinita Ave, Sunnyvale, CA 94085, USA

*skcheme@gmail.com (S.K.); Lei.Cheng2@us.bosch.com (L.C.); haegyumkim@lbl.gov (H.K.);

Supporting Information Includes:

Supplementary Note 1: Details on our theoretical calculation procedure and analysis.

Supplementary Note 2: Details on the precursor test for practical access to the purest $Mg_{1-x}Ti_{2+x}O_5$ (MTO) composites.

Supplementary Note 3: Details on the evaluating entropic contributions in MTO materials.

Figure S1: Chemical representation of interface reactions between the adsorbate and substrate.

Figure S2: DFT slab models that are used in materials screening for finding anti-corrosive and conductive oxide materials.

Figure S3: Chemical representation of single-atom adsorption on the substrate.

Figure S4: Correlations between two DFT calculated physical descriptors.

Figure S5: Hydrogen dissociation on MTO, TiO_2, and TiO slab models.

Figure S6: Total Density of States (DOS) for various oxide compounds.

Figure S7: XRD results on the products from different precursors:

Figure S8: Rietveld-refined XRD profiles and refined lattice constants of the purest MTO phases synthesized under different gas environments.

Figure S9: Relation between powder color and average valence state changes of Ti by the gas environment.

Figure S10: XRD results of the temperature and environmental controlled test.

Figure S11: SEM image and particle size analysis results of $Mg_{1-x}Ti_{2+x}O_5$ powder.

Figure S12: Artifacts on XPS results during Ar etching.

Figure S13: Structural analysis before and after the acid test of MTO.

Figure S14: Configurational entropy for MTO materials.

Figure S15: Interfacial reactivity for MTO materials exposed to acidic environments.

Figure S16: XRD results of the repetitive heating test.

Table S1. Single-atom DFT adsorption energies and experimentally measured conductivity values on various slab models for understanding chemical reactivity.

Table S2. Rietveld refinement driven from the experimental results.

Supplementary Note 1

The search for chemically protective oxides is being performed with first-principles density functional theory (DFT) calculations by creating an interface between the adsorbing corrosive chemical molecule such as H_3O^+, HF, OH^-, and/or SO_3^- and the oxide substrate DFT slab models. These four chemical species, in particular, are commonly present in the acidic proton-exchange fuel cell (PEMFC) environment that may degrade or corrode metallic subcomponents. In **Figure S1**, we provide a schematic view of H_3O^+ adsorbate molecule on the RuO_2 surface slab model. A chemisorption reaction occurs as H_3O^+ approaches RuO_2, followed by a dissociation reaction, as shown in **Figure S1**. During the dissociation reaction, the oxygen atom in H_3O^+ dissociates on surface Ru atom and the hydrogen atom dissociates on surface oxygen atom of RuO_2. Therefore, a single-atom adsorption tendency of an anion on a surface atom and/or a cation on a surface oxygen atom may be able to capture the thermodynamic energetics for a full chemical reaction that will be discussed at subsequent section.

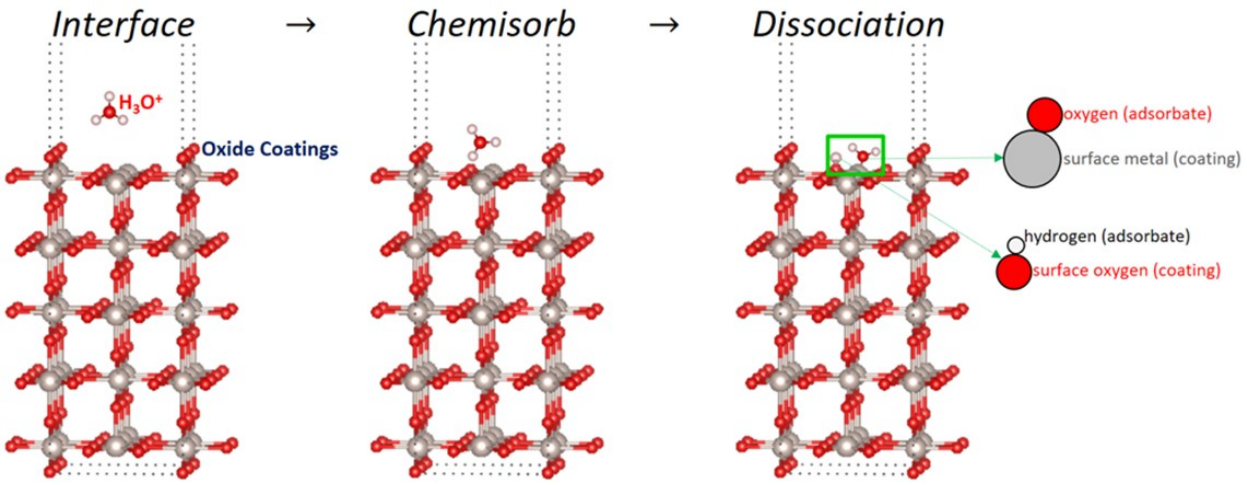

Figure S1. Chemical representation of interface reactions between the adsorbate (H_3O^+) and substrate (RuO_2). Initially, adsorption will take a place at the most favorable site – *i.e.,* here, hydrogen atom in H_3O^+ approaching the surface oxygen in RuO_2 slab. Then, a dissociation step may take a place, where anion from the adsorbate (here, oxygen in H_3O^+) will react at the surface Ru site in RuO_2 slab model. These reactions between the adsorbate and substrate can be also represented and correlated by the combination of two simplified single-atom DFT adsorption calculations, *i.e.*, testing H adsorption on the surface oxygen of RuO_2 slab and O adsorption on the surface Ru metal of RuO_2 slab, as shown in the right panel.

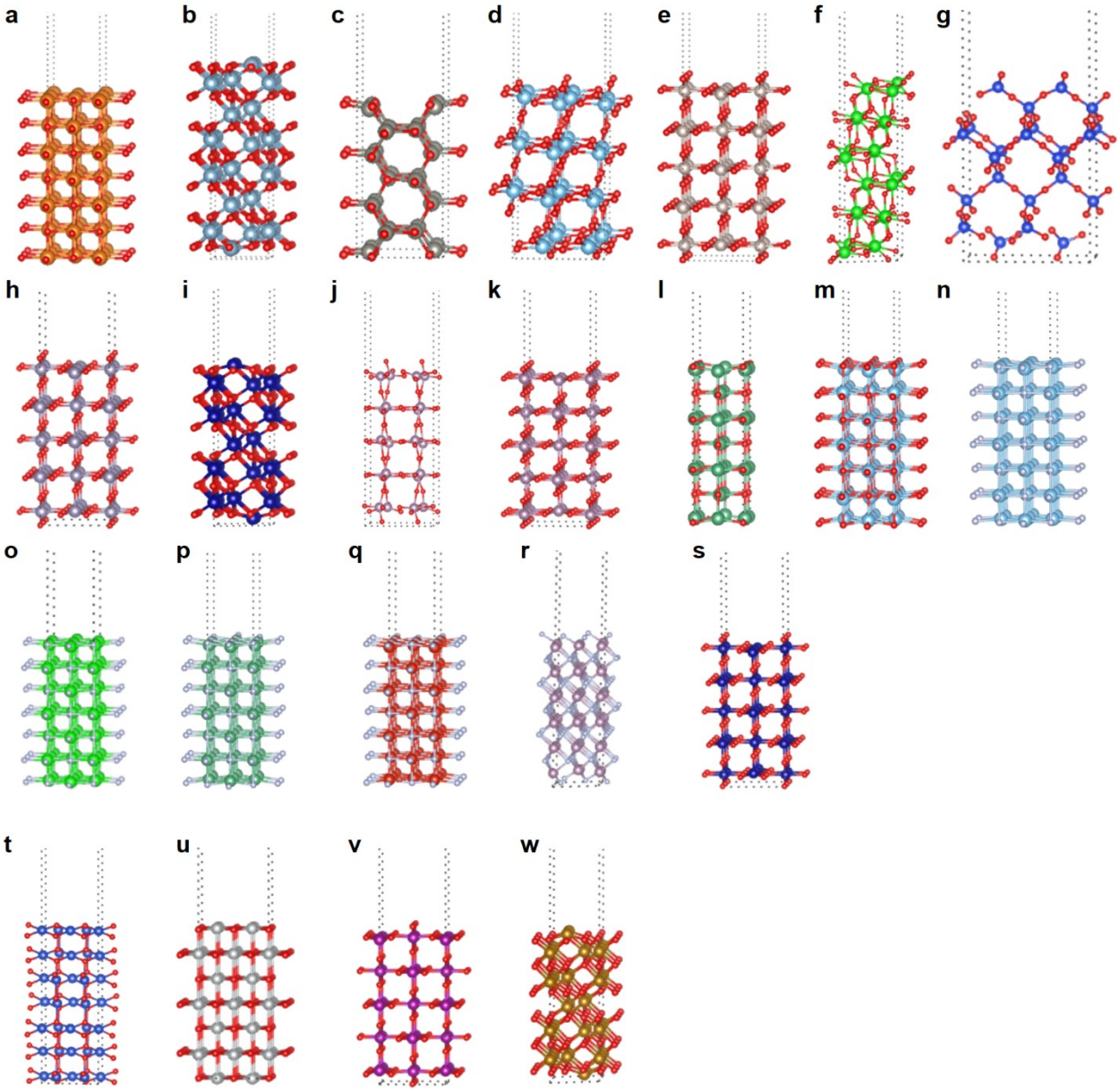

Figure S2. DFT slab models that are used in materials screening for finding anti-corrosive and conductive oxide materials. The chemical structures of: (a) 001 MgO, (b) (001) Al_2O_3, (c) (110) ZnO, (d) (101) TiO_2, (e) (110) RuO_2, (f) (-111) ZrO_2, (g) (001) SiO_2, (h) (110) SnO_2, (i) (001) Cr_2O_3, (j) (010) MoO_3, (k) (110) MoO_2, (l) (001) NbO, (m) (001) TiO, (n) (001) TiN, (o) (001) ZrN, (p) (001) NbN, (q) (001) VN, (r) (001) MoN, (s) (110) CrO_2, (t) (111) CuO, (u) (100) NiO, (v) (110) MnO_2, and (w) (001) Fe_2O_3. The energetically-stable surface facet – known from experiment and/or computation – is chosen to evaluate the chemical reactivity against the corrosive species. We make a simple assumption that oxide materials will preferentially grow in its most energetic surface facet.

Next, we have prepared 23 different binary oxides and nitrides slab models. For each system, we choose the most energetically-stable surface facet, according to experimentation and/or computations, as follows: (001) MgO, (001) Al_2O_3, (101) TiO_2, (-111) ZrO_2, (110) ZnO, (110) SnO_2, (001) Cr_2O_3, (010) MoO_3, (110) MoO_2, (001) NbO, (001) TiO, (001) TiN, (001) ZrN, (001) NbN, (001) VN, (001) MoN, (110) CrO_2, (110) RuO_2, (111) CuO, (100) NiO, (110) MnO_2, (001) SiO_2, and (001) Fe_2O_3. Based on a simple assumption that materials will preferentially grow its most energetic surface facet, we believe that our DFT slab models are sufficient to accurately understand chemical reactivity of materials. In **Figure S2**, we have provided the chemical structures of DFT slab models.

With 23 different binary oxides and nitrides DFT slab models, we test the chemical reactivity for each material using a single-atom adsorption calculation as depicted in **Figure S3**. As discussed earlier in **Figure S1**, this is an accelerated approach with using a single atom that can correlate H for H_3O^+, F for HF, S for SO_3^-, and O for OH^-, *etc.* For all slab models, we use the sufficient vacuum thickness of at least 12 Å.

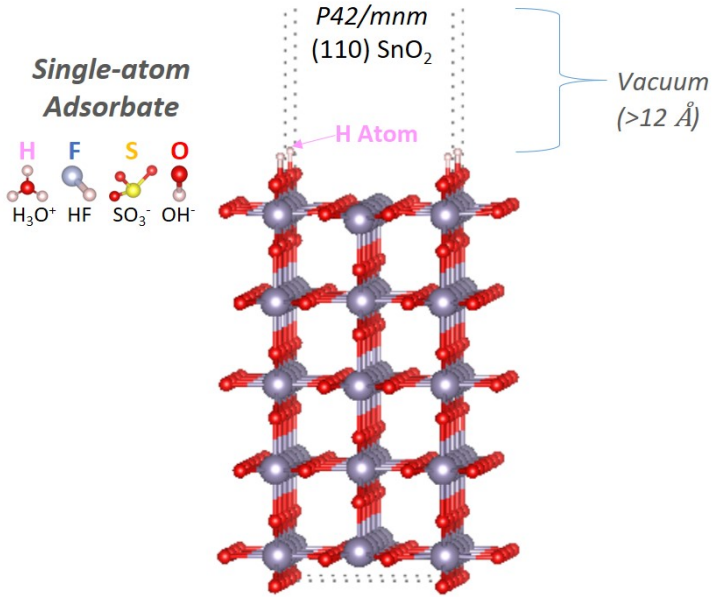

Figure S3. Chemical representation of single-atom adsorption on the substrate. Here, we show a single H atom adsorption (*i.e.*, representing H_3O^+ adsorption) on (110) SnO_2 DFT slab structure. We further have studied F, S, and O adsorptions (*i.e.*, representing HF, SO_2/SO_3, and OH dissociation reactions). Lastly, we have examined the anion vacancy formation energy in each slab model by removing a surface oxygen or a nitrogen atom to understand the chemical stability in reducing conditions (*e.g.*, MO_2 becoming MO_{2-x}).

Table S1. Single-atom DFT adsorption energies on various slab models for understanding chemical reactivity. We also provide the anion vacancy formation energies. The units for adsorption and vacancy formation energies are eV. The approximate range of experimental conductivities are provided in the last column.

Surface	$\Delta E_{H,ads}$ [eV]	$\Delta E_{F,ads}$ [eV]	$\Delta E_{O,ads}$ [eV]	$\Delta E_{S,ads}$ [eV]	$\Delta E_{O(N),vac}$ [eV]	*Exp.* σ [S/cm]	Ref	Note
(001) MgO	1.965	0.460	2.743	1.147	6.585	$\sim10^{-10}$	[1]	
(001) Al_2O_3	1.570	-2.739	1.194	1.922	6.073	$\sim10^{-15}$	[1]	Protective, but insulating
(101) TiO_2	0.039	-1.410	1.758	2.262	5.010	$\sim10^{-12}$	[2]	
(-111) ZrO_2	0.961	-1.885	0.091	0.481	6.493	$\sim10^{-9}$	[3]	
(110) ZnO	0.071	-1.583	1.606	0.459	3.165	$\sim10^{-7}$	[2]	
(110) SnO_2	-1.364	-1.791	2.174	2.434	2.671	$\sim10^{-7}$	[2]	
(001) Cr_2O_3	0.595	-4.279	-3.237	-0.969	5.415	$\sim10^{-6}$	[4]	Less protective, but moderately conductivity
(010) MoO_3	-1.526	-1.984	0.208	1.775	0.260	$\sim10^{-5}$	[5]	
(110) MoO_2	0.096	-4.401	-3.685	-1.266	5.011	$\sim10^{0}$	[5]	
(001) NbO	1.172	-5.210	-4.378	-2.236	5.770	$\sim10^{4}$	[6]	
(001) TiO	0.763	-2.155	-4.633	-5.165	4.899	$\sim10^{2}$	[7]	
(001) TiN	0.400	-4.487	-3.197	-0.822	3.013	$\sim10^{5}$	[8]	Not very protective, but conducting
(001) ZrN	0.588	-5.089	-3.495	-1.385	3.323	$\sim10^{5}$	[8]	
(001) NbN	0.321	-4.478	-4.075	-1.558	2.031	$\sim10^{4}$	[8]	
(001) VN	0.106	-3.704	-3.307	-0.786	1.659	$\sim10^{5}$	[8]	
(001) MoN	-0.956	-4.245	-4.048	-2.582	1.507	$\sim10^{4}$	[5]	
(110) CrO_2	-1.140	-2.758	-1.313	0.947	2.422	$\sim10^{2}$	[9]	
(110) RuO_2	-0.997	-3.123	-1.363	0.179	2.989	$\sim10^{4}$	[2]	
(111) CuO	-0.954	-2.703	0.384	2.074	2.592	$\sim10^{-10}$	[2]	Not advantageous
(100) NiO	-0.254	-3.229	-0.615	0.247	2.577	$\sim10^{-15}$	[2]	
(110) MnO_2	-1.539	-2.200	-0.218	1.430	1.793	$\sim10^{-11}$	[4]	
(001) SiO_2	-0.175	-3.306	-0.616	-0.009	3.135	$\sim10^{-14}$	[10]	

(001) Fe_2O_3	-0.009	-4.013	-2.053	-0.713	2.938	$\sim 10^{-7}$	[11]

Table S1 provides DFT single-atom adsorption energies of H, F, O, and S for 23 DFT slab models. The DFT single-atom adsorption energies of H, F, O, and S are found in the columns named $\Delta E_{H,ads}$, $\Delta E_{F,ads}$, $\Delta E_{O,ads}$, and $\Delta E_{,S,ads}$, respectively. Here, a positive DFT adsorption energy indicates a high stability of the coating material (*i.e.*, it costs energy for a reaction to occur), while a negative DFT adsorption energy indicates that the coating material and the adsorbate would react (*i.e.,* a spontaneous reaction). **Table S1** also includes the surface oxygen or nitrogen vacancy formation energy ($\Delta E_{O(N),vac}$) calculation results, where this value indicates the energy penalty to remove a surface anion from the substrate material. Having a high oxygen or nitrogen vacancy formation energy typically leads to a higher chemical stability – *i.e.*, less dissolution, decomposition, *etc.*

According to **Table S1**, (001) SiO_2 and (110) MnO_2 have all negative adsorption energies. These calculations align with the known experimental data demonstrating that SiO_2 and MnO_2 react with HF, H_2SO_4, and other acids very favorably. We use the calculation results in **Table S1** to categorize 23 oxides and nitrides into four categories: *i*) protective but insulating; *ii*) less protective but moderately conducting; *iii*) not very protective but conducting; and, *iv*) not advantageous.

The following oxides fall into the first category (*i.e.*, protective, but insulating): MgO, Al_2O_3, TiO_2, and ZrO_2. These materials have three to four positive adsorption energies in **Table S1** that are considered to be very protective but usually insulating. The following oxides fall into the second category (*i.e.*, less protective but moderately conducing): ZnO, SnO_2, Cr_2O_3, MoO_3, and MoO_2, where they are found to be moderately conducting. Regarding the protection, these materials at least have a positive value of $\Delta E_{H,ads}$; or, in addition, have 2 or more positive values among calculated adsorption energies. The following oxides and nitrides fall into the third category (*i.e.*, not very protective but conductive): NbO, TiO, TiN, ZrN, NbN, and VN. They have at least one positive adsorption energies in **Table S1**. The rest of materials tested are found to be not very advantageous. For example, MoN, CrO_2, and RuO_2 are conductive but not chemically protective; and CuO, NiO, MnO_2, SiO_2, and Fe_2O_3 are not protective nor conductive. CuO has two positive adsorption energies (stability against OH^- and SO^{3-}, but $\Delta E_{OH,ads}$ is close to zero) and two negative adsorption energies (reacting with H_3O^+ and HF), and therefore it is considered for the fourth

category.

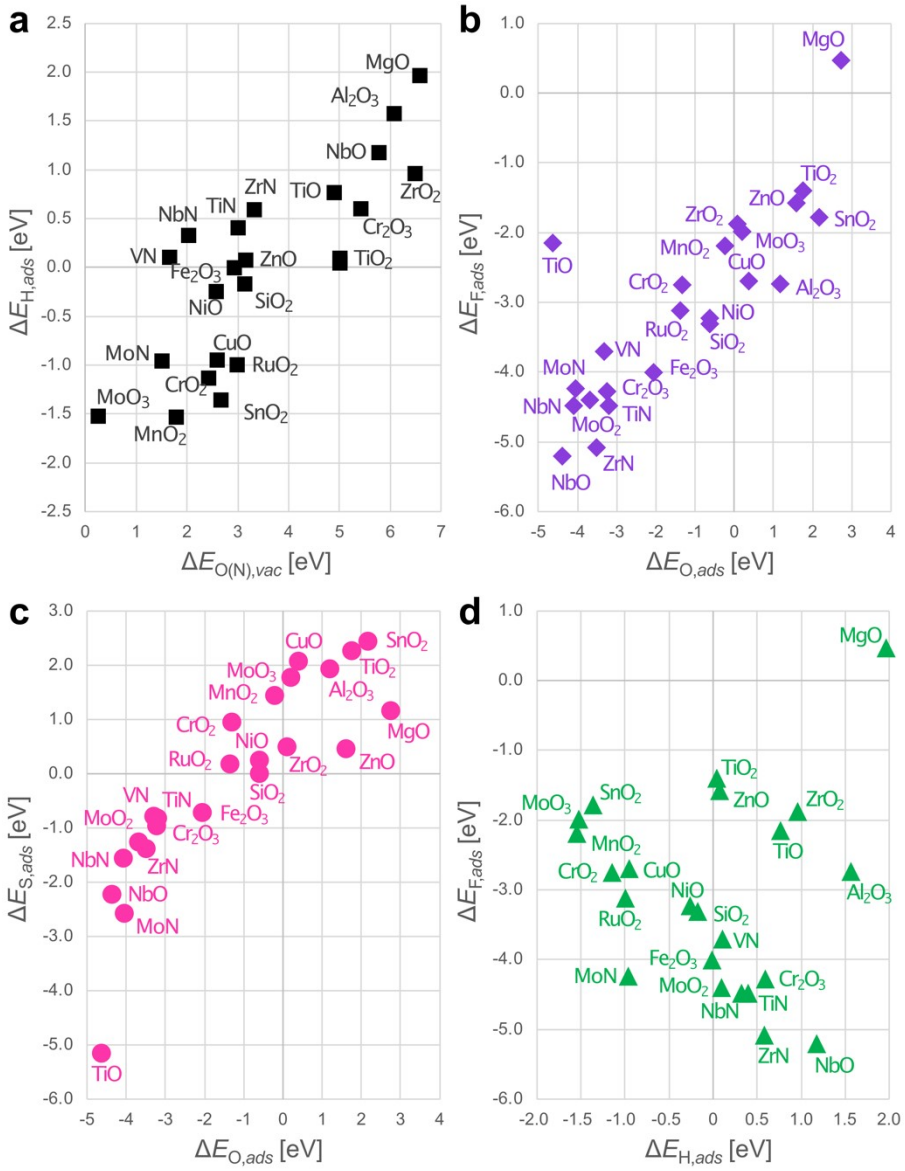

Figure S4. Correlations between two DFT calculated physical descriptors. (a) $\Delta E_{O(N),vac}$ *vs.* $\Delta E_{H,ads}$, (b) $\Delta E_{O,ads}$ *vs.* $\Delta E_{F,ads}$, (c) $\Delta E_{O,ads}$ *vs.* $\Delta E_{S,ads}$, and (d) $\Delta E_{H,ads}$ *vs.* $\Delta E_{F,ads}$.

In **Figure S4**, we observe that a first DFT single-atom adsorption energy ($\Delta E_{x,ads}$) can be correlated to a second DFT single-atom adsorption energy ($\Delta E_{y,ads}$), or an anion surface DFT vacancy formation energy ($\Delta E_{O(N),vac}$). **Figure S4a** shows $\Delta E_{H,ads}$ as a function of $\Delta E_{O(N),vac}$ for 23

oxides and nitrides tested in **Table S1**. **Figure S4b** plots $\Delta E_{F,ads}$ as a function of $\Delta E_{O,ads}$. **Figure S4c** graphs $\Delta E_{S,ads}$ as a function of $\Delta E_{O,ads}$. Lastly, we plot $\Delta E_{F,ads}$ *vs.* $\Delta E_{H,ads}$ in **Figure S4d**. Most protective materials are located on the upper right corner in each plot with higher DFT binding energies. Also, there are "acceptable" correlations found in **Figures S4**, which indicates one or two DFT quantities might be "sufficient" for predicting the chemical stabilities of materials.

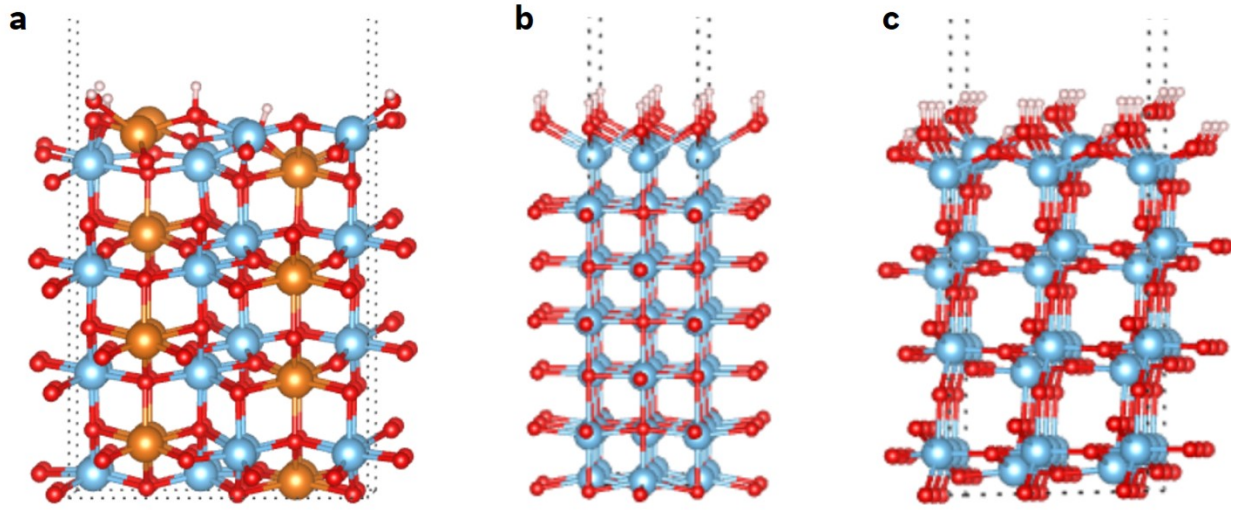

Figure S5. Hydrogen dissociation on (a) (110) $MgTi_2O_5$, (b) (100) TiO, and (c) (101) TiO_2 slab models. It is possible to observe for TiO and TiO_2, hydrogen atom attaches to all oxygen atoms (*i.e.*, surface hydrogen coverage of 100%). In contrast, for the $MgTi_2O_5$, we find from our DFT calculations that hydrogen adsorption does not happen at all oxygen sites, *i.e.*, surface hydrogen coverage of 30.8% - more protective in acidic environment. We find the hydrogen dissociation DFT energy for $MgTi_2O_5$, TiO, and TiO_2 are similar, at ~1 eV/H.

According to our theoretical analysis, we are proposing a new hypothesis that Mg-Ti-O compound may lead to both anti-corrosive and conductive behaviors, if the surface nature of Mg-O and Ti-O octahedrons can be preserved in the ternary compound. Among different Mg-Ti-O compounds, we chose a Ti-excess $MgTi_2O_5$ (orthorhombic, *Cmcm*) as the model system in this work. In **Figure S5**, we have further tested hydrogen dissociations on $MgTi_2O_5$, TiO, and TiO_2 slab models, where we expect testing hydrogen dissociations on these model systems should be sufficient to predict the chemical stabilities, as discussed above in **Figure S4**. As shown in **Figure 1b,** while the calculated hydrogen dissociation energy ($\Delta E_{diss,H}$) for $MgTi_2O_5$, TiO, and TiO_2 are

similar to each other (*i.e.*, ~1 eV per site), the hydrogen coverage on the (110) $MgTi_2O_5$ surface is significantly less than (100) TiO and (101) TiO_2. Here, we define the hydrogen coverage as the ratio between hydrogen adsorbate atoms to the number of available surface oxygen sites in metal oxides. A significantly reduced hydrogen coverage of ~30% is found for $MgTi_2O_5$, while the hydrogen coverage for TiO and TiO_2 is found to be 100%. Our theoretical results indicate that if there are the same number of corrosive species present in the surrounding, the tendency for the corrosive species to bind onto $MgTi_2O_5$ is significantly less, when compared to TiO and TiO_2.

We further examine the electronic structures of MgO, TiO, $MgTi_2O_5$, $MgTi_2O_{4.92}$, $Al_{0.08}Mg_{0.92}Ti_2O_5$, and $Mg_{0.73}Ti_{2.27}O_5$ in **Figure S6** by calculating the density of states (DOS). It is possible to determine in **Figure S6** that while MgO and $MgTi_2O_5$ are insulators, TiO is found to be metallic (*i.e.*, Fermi level (E_F) is being occupied at x = 0). We find that the electronic structures can be tuned to become metallic for: *i*) oxygen deficient MTO, *ii*) Al-doped MTO in Mg site, and *iii*) Ti-excess MTO, as shown in **Figures S6d-f**.

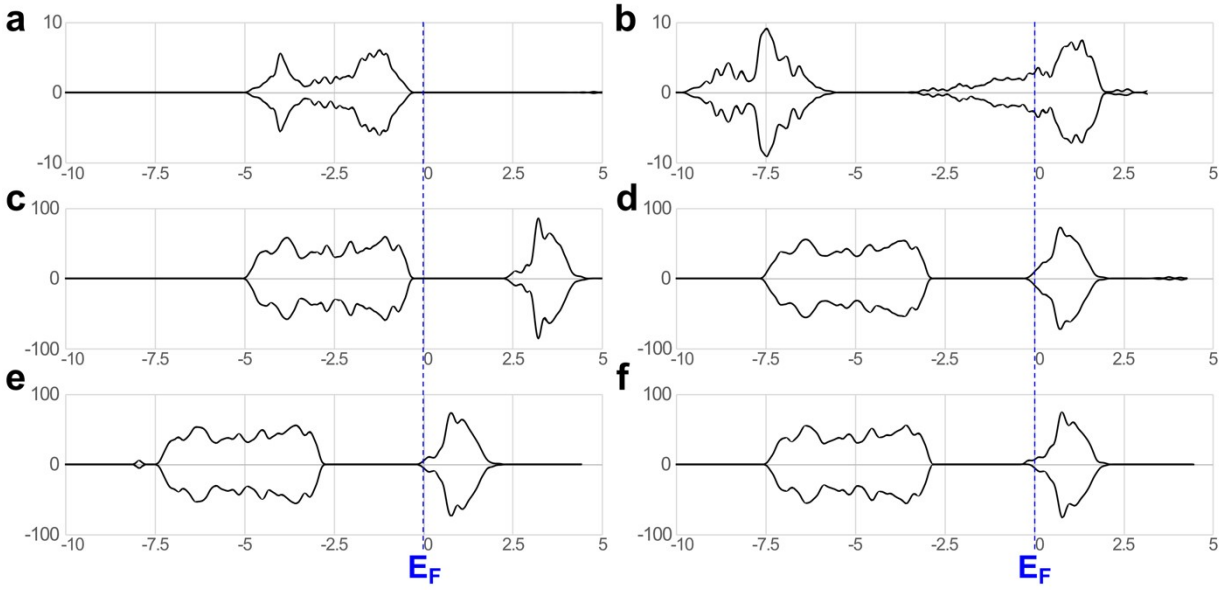

Figure S6. Total Density of States (DOS) for: (a) MgO, (b) TiO, (c) $MgTi_2O_5$, (d) $MgTi_2O_{4.92}$, (e) $Al_{0.08}Mg_{0.92}Ti_2O_5$, and (f) $Mg_{0.73}Ti_{2.27}O_5$. The Fermi level (E_F) is set at $x = 0$

Supplementary Note 2

To choose the proper precursors for practical access to the Mg-Ti-O ternary compound, we first test various precursors of Mg and Ti. **Figure S7** shows the XRD results on the synthesized MTOs from different precursors. The use of TiO precursor fails to form $MgTi_2O_5$, rather form Mg_2TiO_4. Ti_2O_3 and TiO_2 can make $MgTi_2O_5$ with impurities (e.g., Mg_2TiO_4), and TiO_2 showed the least Mg_2TiO_4 impurities among the Ti precursors we tested. For the Mg precursors, $MgCO_3$ showed to form $MgTi_2O_5$ with fewer Mg_2TiO_4 impurity, compared to MgO. It suggests that using TiO_2 and $MgCO_3$ as precursor can make the purest phase of $MgTi_2O_5$.

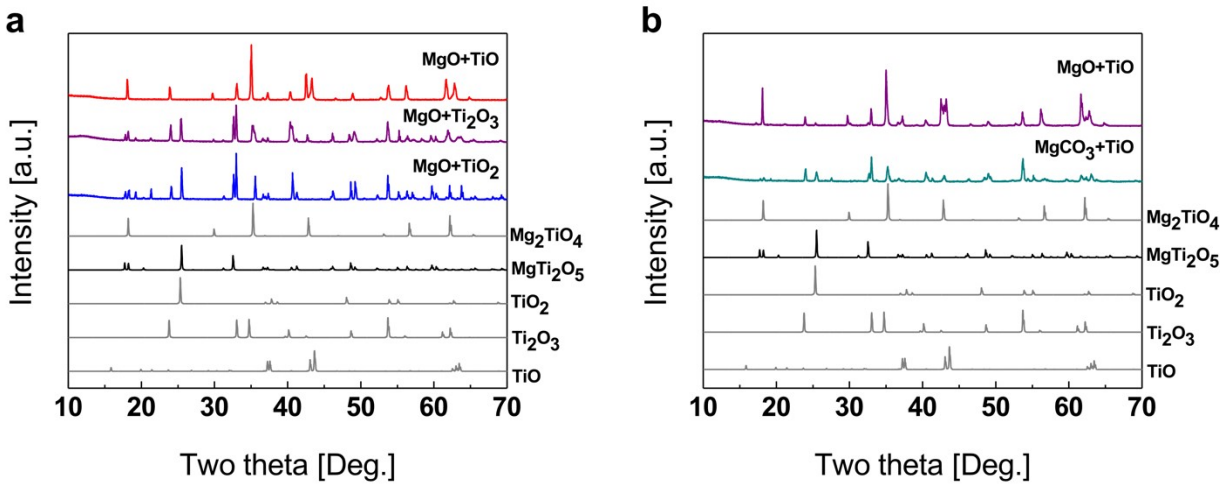

Figure S7. XRD results on the products from different precursors: (a)Ti and (b)Mg.

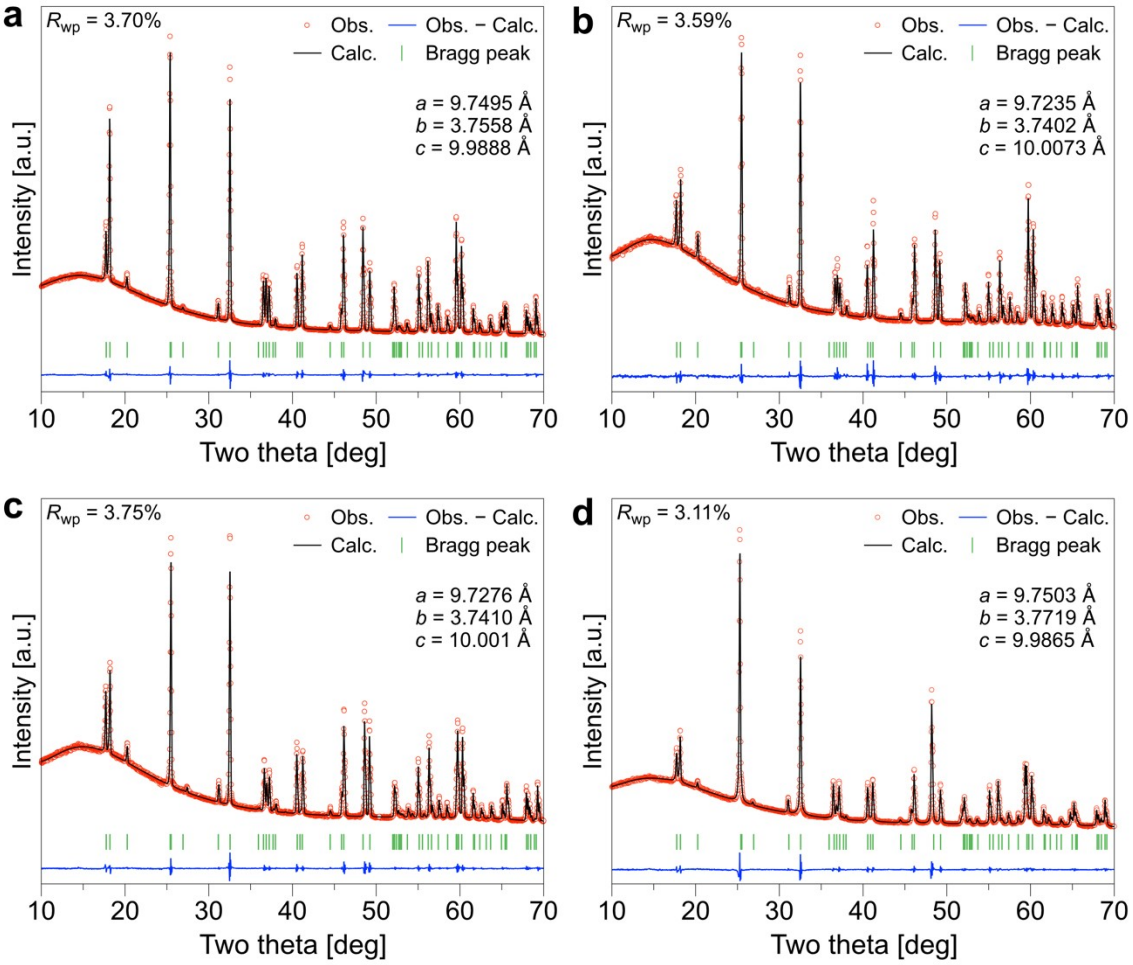

Figure S8. Rietveld-refined XRD profiles and refined lattice constants of (a-c) the purest MTO phases synthesized under different gas environments: (a) 2% H_2/Ar mixed gas (Ti/Mg = 2.3), (b) Ar gas (Ti/Mg = 1.8), and (c) ambient air (Ti/Mg=1.8). (d) Rietveld-refined XRD profile of the MTO, synthesized from 2% H_2/Ar mixed gas (Ti/Mg = 4.0), exhibited the highest conductivity (6.09×10^{-1} S cm), where Ti valence (3.65+) corresponding to $Mg_{0.57}Ti_{2.43}O_5$. Note that a,b, and c are the refined lattice constants and R_{wp} is a weighted profile R-factor of the refinement.

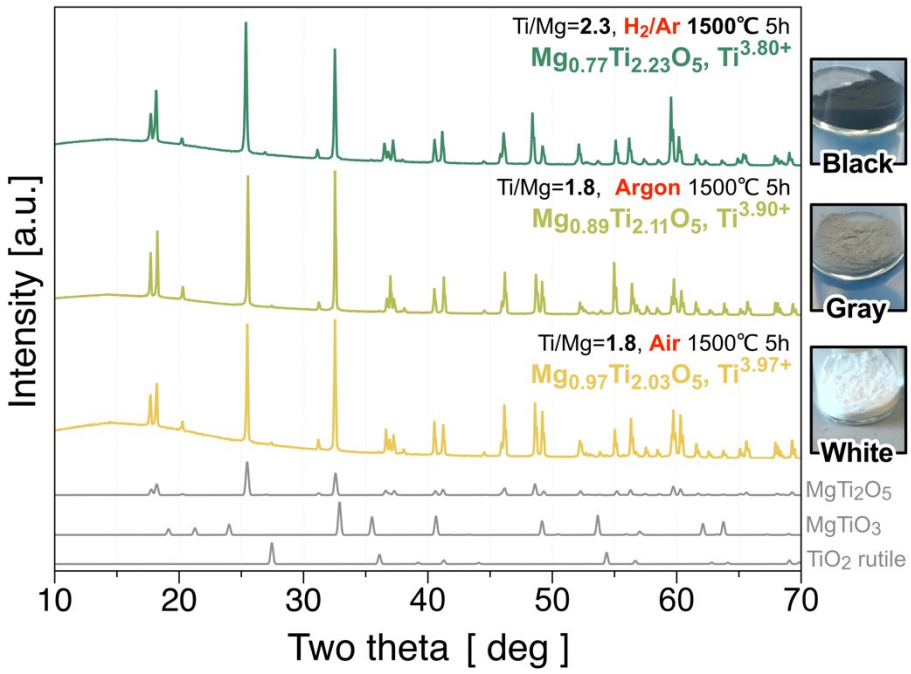

Figure S9. Relation between powder color and average valence state changes of Ti by the gas environment.

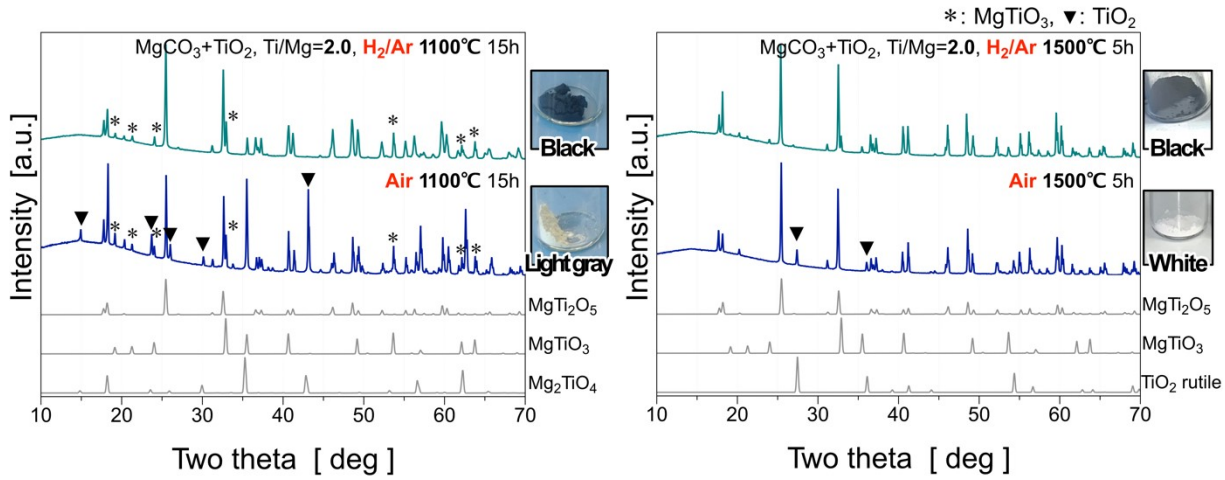

Figure S10. XRD results and powder color changes observed in the temperature and environmental controlled test: 1100℃ vs. 1500℃ and 2% H_2/Ar mixed gas vs. ambient air

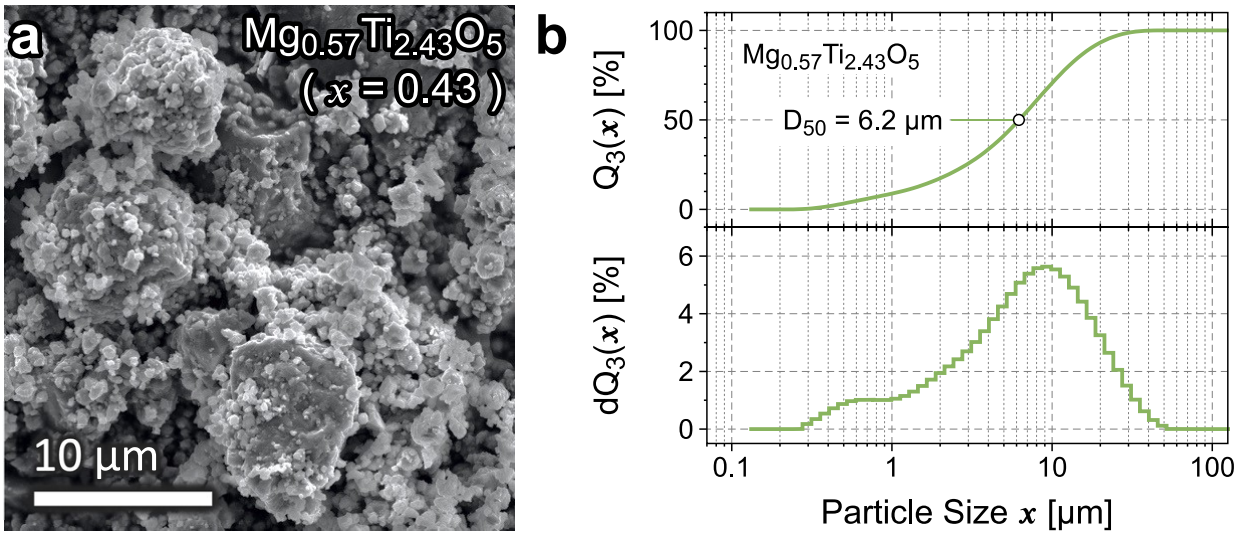

Figure S11. (a) SEM image and (b) particle size analysis results of $Mg_{0.57}Ti_{2.43}O_5$ (x = 0.43, where $Mg_{1-x}Ti_{2+x}O_5$) powder. Note that the typically hand-ground MTO particles have 5-10 μm in average sizes, which makes SEM-EDS measurements on the powders collect the information at surface-wise, not bulk region.

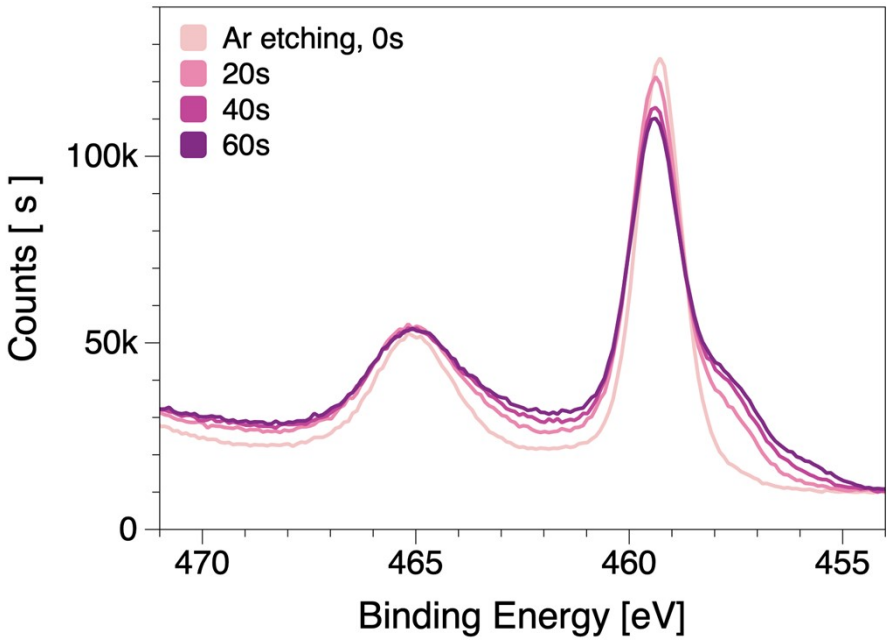

Figure S12. Artifacts on XPS results during Ar etching. Ti-L edge XPS spectra were measured after 0, 20, 40, and 60 sec of Ar etching, respectively. It is clearly shown that the Ti 2p3/2 peaks (~459 eV) shifted as the Ar^+ ion beam irradiates, and the reduction intensity (shoulder at ~457 eV) increases. Considering the reduction environment (H_2/Ar) during the sintering and the EELS results shown in **Figure 5e**, this reduction inside mainly comes from the Ar beam-induced reduction, not reflecting the synthesized characteristics.

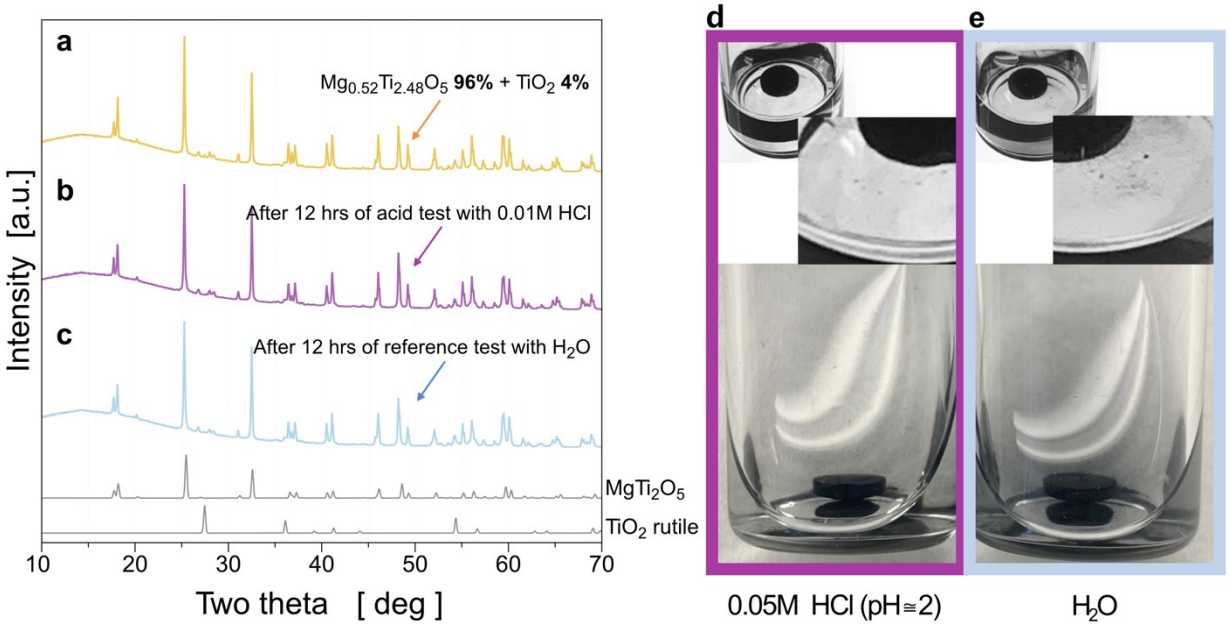

Figure S13. (a-c) Structural analysis of (a) as synthesized MTO ($Mg_{0.52}Ti_{2.48}O_5$) from Ti/Mg=4.0 precursor, (b) after 12 hours of the acid test with 0.01M HCl (pH ≅ 1.0), and (c) after 12 hours of the reference test with H_2O. (d-e) Optical micrographs showing the physical tear-off of the MTO pellets after each test (b and c), respectively. Considering the minor differences between the XRD results of (a-c), we concluded the debris observed in the liquid (d-e) is not related to the structural degradation but only be the physically tear-offed particles from the MTO pellet.

Supplementary Note 3

Here we analyze the entropic contributions in MTO materials. We consider a material $Mg_{1-x}Ti_{2+x}O_5$ where there are 1 M1 site and 2 M2 sites per formula unit, and where the crystal geometry exhibits an enthalpic preference for Ti in M2 sites and Mg in M1 sites. The entropy of disorder depends both on x (excess Ti) and on a disorder parameter ξ, ranging from ξ=1 (random ordering) to the ordered ξ=0, where Mg (Ti) is in M1 (M2) sites as much as possible. These extrema are illustrated in the occupancies of **Figure S13a**; for ξ=1, the occupancy is given only by the Mg:Ti ratio and the crystal site has no impact, whereas in the ξ=0 case the occupancies are as close to 1.0 as possible. The intermediate values of 0<ξ<1 can be interpolated linearly.

This generates the mixing entropy shown in **Figure S13b** given by $S = -R\sum_i c_i \ln c_i$. At high values of disorder (ξ~1), the entropy is dominated by the Ti:Mg balance, whereas for mostly ordered structures (ξ~0), the entropy spikes sharply near x=0. Experimental Rietveld refinement (Table S2) indicates our MTO structures have almost 100% occupancy of M2 by Ti, indicating the ξ=0 limit is the appropriate quantity to use.

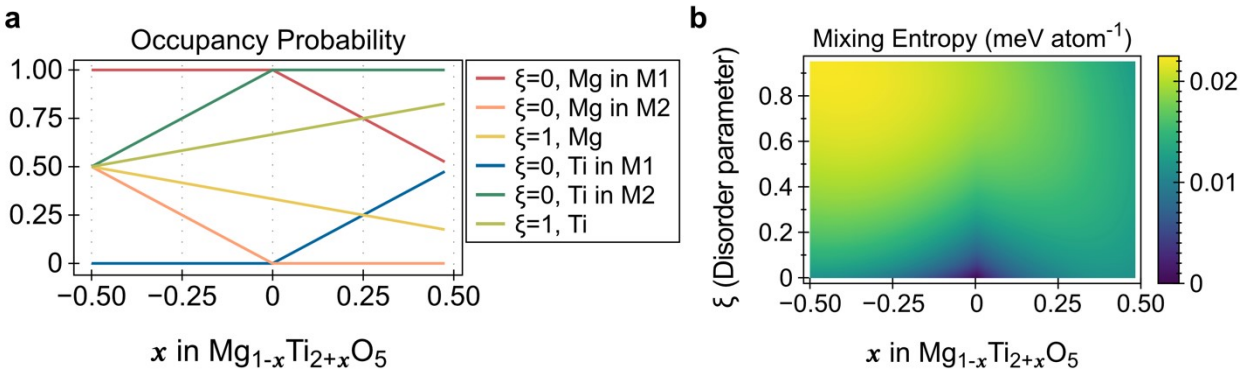

Figure S14: (a) The probability of a species Mg or Ti occupying the M1 and M2 sites. In ξ=0, a fully ordered (enthalpy-driven) case, the Mg (Ti) strongly prefers M1 (M2) and only excess ions change the occupancy. But in ξ=1, a fully random case, the ordering is entirely random and depends only on the Mg:Ti ratio. (b) The corresponding mixing entropy scaling from ordered to disordered materials.

Table S2. Rietveld refinement driven from the experimental results.

x in $Mg_{1-x}Ti_{2+x}O_5$	a (nm)	b (nm)	c (nm)	Ti occupancy in M1 site	Ti occupancy in M2 site
0.14	0.97388	0.37527	0.99985	0.1371 (Mg: 0.8629)	1.0000 (Mg:0)
0.32	0.97422	0.37561	0.99952	0.3203 (Mg: 0.6797)	1.0000 (Mg:0)
0.43	0.97623	0.37717	0.99876	0.4255 (Mg:0.5745)	1.0000 (Mg:0)
0.59	0.97691	0.37716	0.99873	0.5945 (Mg: 0.4055)	1.0000 (Mg:0)

In an acidic environment, the material undergoes an electrochemical corrosion reaction similar to

$$e^- + H_3O^+ + Mg_{1-x}Ti_{2+x}O_5 \rightarrow byproducts$$

with the reactants dependent on the acid concentration used. By entropically stabilizing the MTO on the reactant side, the energy of the reaction is lowered, thus reducing the likelihood of corrosion. Unfortunately, computational electrochemistry struggles to quantitatively predict the energy of such a reaction, and therefore we ultimately must rely on experiment to find the optimal value of *x* that prevents corrosion. This issue is further exacerbated by the reliance of the corrosion energy on the surface structure, including the hydrogen coverage, surface oxidation, and charge state, as measured and described in the main text.

Nonetheless, we can use computational techniques to justify that an entropic contribution is of the correct order of magnitude to stabilize the off-stoichiometric MTO we analyze here. Using the standard interface stability techniques,[12, 13] we compute the interfacial reaction enthalpy of the non-electrochemical partner reaction

$$H_3O + Mg_{1-x}Ti_{2+x}O_5 \rightarrow byproducts$$

As shown in **Figures S15a-b**, the reaction enthalpies for x>0 are entirely negative (unstable), corresponding to a susceptibility to corrosion. However, when we add the room-temperature entropy contribution of the reactant side, the free-energy landscape alters dramatically. **Figures S8c-d** indicates that for very small amounts of H_3O and/or small values of *x*, the free energy is positive, leading to enhanced stability.

As mentioned, this only indicates that the thermal considerations might stabilize the MTO material, but the electrochemical quantitative amounts are not captured by this analysis. The experimental data in the main text indicate that for our processing method and corrosion surface, the optimal value is $x \approx 0.30$ (see **Figure 6** in the main text).

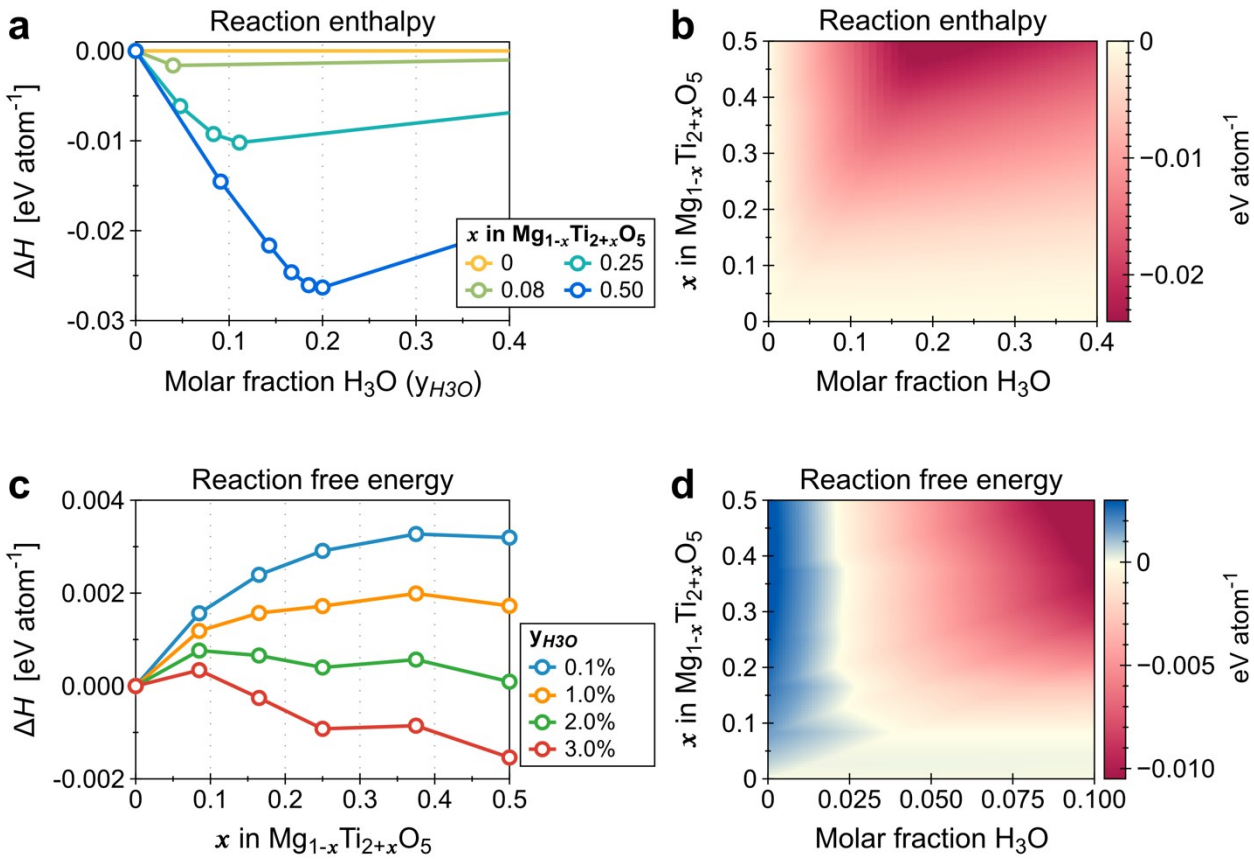

Figure S15. The interface reaction enthalpy and free energy for MTO/H_3O reactivity, as an approximation for the corrosion stability of MTO. The entropic contributions stabilize the MTO interface, especially for small amounts of H_3O and excess Ti. The true susceptibility depends on the surface structure and was investigated experimentally.

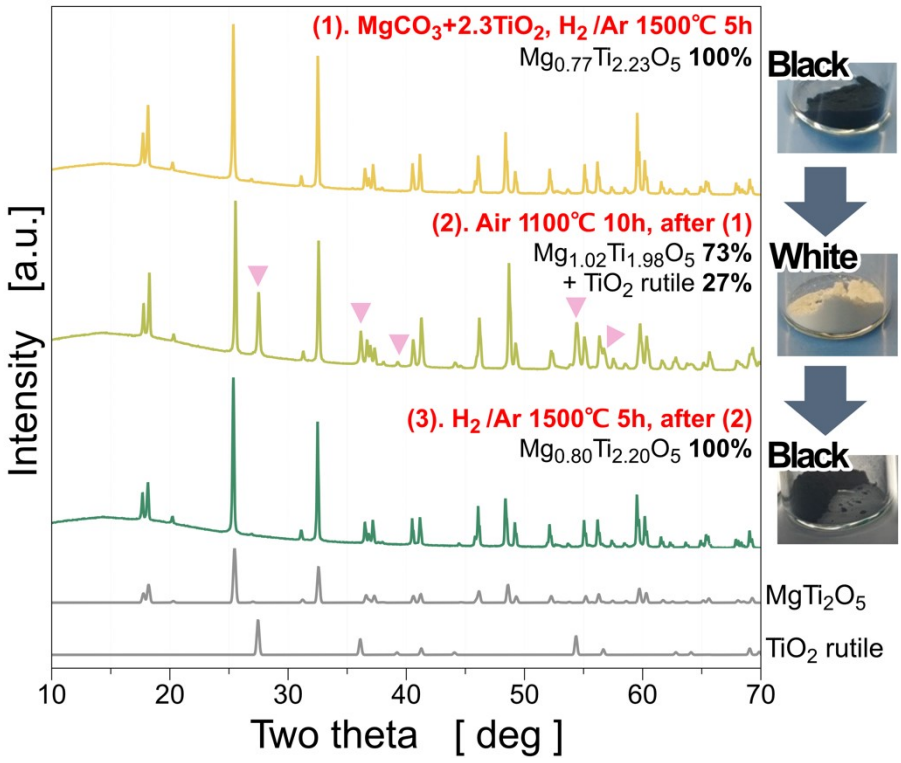

Figure S16. XRD results and powder color changes observed in the repetitive heating test. (1) synthesized MTO from Ti/Mg=2.3 precursor mixture, sintered at 1500℃ for 5 hours under H_2/Ar mixed gas flow. (2) Subsequently sintered MTO under ambient air at 1100℃ for 10 hours. (3) re-sintered MTO under H_2/Ar mixed gas flow, at 1500℃ for 5 hours. Note that the pink triangles in (2) refer to TiO_2 rutile phase.

References

1. T. Tanifuji, Y. Katano, T. Nakazawa and K. Noda, *J Nucl Mater*, 1998, **253**, 156-166.

2. C. N. R. Rao and G. V. Subba Rao, *Phys Status Solidi*, 1970, **1**, 597-652.

3. K. Apriany, I. Permadani, D. G. Syarif, S. Soepriyanto and F. Rahmawati, *Iop Conf Ser Mater Sci Eng*, 2016, **107**, 012023.

4. K. Conder, *Paul Scherrer Institute, Switzerland*, 2012, 1-44.

5. W. Ji, R. Shen, R. Yang, G. Yu, X. Guo, L. Peng and W. Ding, *J Mater Chem A*, 2013, **2**, 699-704.

6. C. Nico, T. Monteiro and M. P. F. Graça, *Prog Mater Sci*, 2016, **80**, 1-37.

7. T. Leichtweiss, R. A. Henning, J. Koettgen, R. M. Schmidt, B. Holländer, M. Martin, M. Wuttig and J. Janek, *J Mater Chem A*, 2014, **2**, 6631-6640.

8. P. Patsalas, N. Kalfagiannis, S. Kassavetis, G. Abadias, D. V. Bellas, C. Lekka and E. Lidorikis, *Mater Sci Eng R Reports*, 2018, **123**, 1-55.

9. G. Ertl, *Crit Rev Solid State*, 1982, **10**, 349-372.

10. J. K. Srivastava, M. Prasad and J. B. Wagner, *J Electrochem Soc*, 1985, **132**, 955-963-955-963.

11. B. M. Warnes, F. F. Aplan and G. Simkovich, *Solid State Ionics*, 1984, **12**, 271-276.

12. W. D. Richards, L. J. Miara, Y. Wang, J. C. Kim and G. Ceder, *Chemistry of Materials*, 2016, **28**, 266-273.

13. Y. Xiao, Y. Wang, S.-H. Bo, J. C. Kim, L. J. Miara and G. Ceder, *Nature Reviews Materials*, 2020, **5**, 105-126.